The Earth surface controls the depth-dependent seismic radiation of megathrust earthquakes

Jiuxun Yin[1], **Marine A. Denolle**[1,2]

[1]Department of Earth and Planetary Sciences, Harvard University
[2]Department of Earth and Space Sciences, University of Washington

Key Points:

- Megathrust earthquakes propagate as cracks updip and self-healing pulse downdip due to the realistic Earth surface and structural effects.
- The depth dependence in megathrust earthquake radiation arises from this difference in rupture behavior.
- The realistic structure is necessary to better predict tsunami and strong ground motion hazards.

Corresponding author: Jiuxun Yin, `jiuxun_yin@g.harvard.edu`

Abstract

Megathrust earthquakes exhibit ubiquitous seismic radiation: low frequency seismic energy is emitted from the shallowest portion of the fault whereas high frequency seismic energy is emitted from the deepest part of the fault. A popular interpretation is a systematic variation in frictional properties with depth. We propose instead that the Earth free surface and realistic structure are the main cause for such style in radiation. To support this, we run two-dimensional dynamic rupture simulations in realistic subduction-zone models. We use a P-wave velocity model derived from a tomographic study, derive density from standard empirical relations, and vary S-wave velocity by imposing a realistic model of V_P/V_S ratio in hydrated and damaged. Our simulations show that the effects of free-surface reflections act on the fault to promote the propagation of crack updip while the sharp material contrasts promote the propagation of self-healing slip pulses downdip. This results in the enhancement of high-frequency radiation downdip compared to updip and can sufficiently explain the ubiquitous observations of depth variation in the radiation of megathrust earthquakes. Finally, we emphasize that the realistic structure of subduction zone is necessary for better seismic and tsunami hazard assessment.

Plain Language Summary

The largest earthquakes occur in subduction zones and such "megathrust earthquakes" generate huge ground motions and devastating tsunami waves that threaten the coastal populations. The recent surge of megathrust earthquakes leads to the observation that: i) the updip portion of the fault is where the rupture tends to generate the largest tsunami hazard and low-frequency seismic radiation, whereas the downdip portion is where the rupture tends to generate the strong ground motion felt by the nearby coastal and urban regions. While the most popular explanation is to infer systematic depth-dependent properties on the fault, this study shows that the realistic Earth surface and structural models, which promote the interference between seismic waves and the rupture, are sufficient to explain these observed phenomena.

1 Introduction

The largest and some of the most damaging earthquakes occur offshore in subduction zones: the 1960 Great Chilean Mw 9.4, the 1964 Alaskan Mw 9.3, 2004 Sumatra Mw 9.2, and the 2011 Tohoku Mw 9.0. Almost 1 in 10 people in the world live on the coast. Thus understanding the rupture behavior of megathrust earthquakes is critical for seismic and tsunami risk mitigation in coastal areas. The recent occurrence of multiple of these events has coincided with a vast expansion in seismic networks, which, in turn, has lead to the discovery of a multitude of processes surrounding the rupture of these large earthquakes (Ishii et al., 2005).

A foremost important and ubiquitous observation is that low frequency (LF) seismic radiation is mostly generated at the shallow, updip region, while high frequency (HF) seismic radiation tends to come mostly from the deep, downdip region. We refer to this as the "depth-frequency relation" in this work. This observation is manifested in three ways. First, studies on earthquake source time functions highlight a shortening of the source pulse that is well explained by the increase in elastic properties with depth (Houston, 2001; Vallée, 2013) and an increase in relative contributions of high-frequency radiation at depth along the megathrust (Ye et al., 2016). Second, kinematic studies such as finite fault inversions (Yue et al., 2016) and backprojection images from teleseismic P waves (Kiser et al., 2011; Yao et al., 2013; Melgar et al., 2016; Yin et al., 2016, 2017, 2018) show that, within a single rupture, high frequencies are more efficiently generated at the deep portions of the megathrust rather than its updip end. Third, the strong ground motions that are responsible for building damage may arrive as distinct high-frequency bursts from the downdip of megathrust (Kurahashi & Irikura, 2011; Asano & Iwata, 2012; Frankel, 2013).

The most popular interpretation for these observations is the systematic depth variation in frictional properties that result from increasing temperature and pressure with depth, and associated phase transformation. The argument of a systematic depth variations of fault properties can explain the varying seismicity rates at depth (Scholz, 1998), but has also been widely used to explain the depth-varying seismic radiation of large megathrust earthquakes (Lay et al., 2012; Yao et al., 2013; Yin et al., 2017). To reproduce deep HF radiation in models of an earthquake, dynamic rupture simulations have applied various parameterization of pre-stress or fault strength heterogeneity downdip of the megathrust (Huang et al., 2012; Galvez et al., 2014). A recent and alternative interpretation is that of the systematic increase in P-wavespeeds (V_P) with depth in subduction zones (Sallarès & Ranero, 2019). However, such an argument would also imply other systematic increasing trends with depth that are not always observed within the crust, such as stress drop and scaled energy (Allmann & Shearer, 2009; Denolle & Shearer, 2016).

Another major impact on megathrust earthquake dynamics is the asymmetry of the structure: a shallow dipping fault intersects the Earth free surface and the accretionary and frontal wedge materials (hanging wall) are highly compliant compared to the footwall materials. This particular structure tends to trap seismic waves within the wedge and cause significant dynamic stress perturbations (Brune, 1996; Nielsen, 1998; Oglesby et al., 2000; Ma & Beroza, 2008; Guo et al., 2016; Gabuchian et al., 2017; Tal et al., 2020). Such high stresses can lead to material yielding (Ma & Hirakawa, 2013; Ma & Nie, 2019) or unclamping and flapping of the hanging wall (Brune, 1996; Gabuchian et al., 2017; Tal et al., 2020).

Here, we evaluate the impact of the free surface and a realistic, elastic subduction-zone structure on the rupture dynamics of megathrust earthquakes. We use two-dimensional (2D) dynamic models to investigate the radiation style of subduction-zone earthquakes in realistic Earth structure. A related study by Lotto et al. (2017, 2018) performed a similar exercise, albeit a simplification of the 2D elastic structure. This contribution builds upon these studies by using a tomography-derived elastic model, a realistic model of the shear wavespeed (V_S) structure, and a systematic analysis of the seismic waves generated by these ruptures. Regardless of the modeling settings, all simulations can explain the observations: HF seismic waves are more efficiently generated at depth, LF seismic waves are more efficiently generated near the trench. Therefore, the Earth free-surface effect is the dominant factor to control the depth-frequency relation. Furthermore, the difference in radiation style is intensified in realistic Earth models. The subduction of a cold hydrated slab produces a strong material contrast across the plate interface or fault, which favors pulse-like rupture propagation and enhances high-frequency strong ground motions from the downdip region in proximity of the coast. We conclude that modeling earthquake with a realistic Earth is necessary to better predict tsunami height and coastal ground motions.

2 Methods

We perform dynamic rupture modeling in 2D media. We gradually increase structural complexity from homogeneous to realistic elastic structures and from small to large earthquakes. Finally, we analyze the spectral properties of the rupture slip history, the nearby ground motions, and the tsunami potential.

2.1 Representing a realistic megathrust structure

We choose the Tohoku region in northeastern Japan as our study case. We increase the complexity of the medium from a homogeneous half-space with a planar shallow dip-

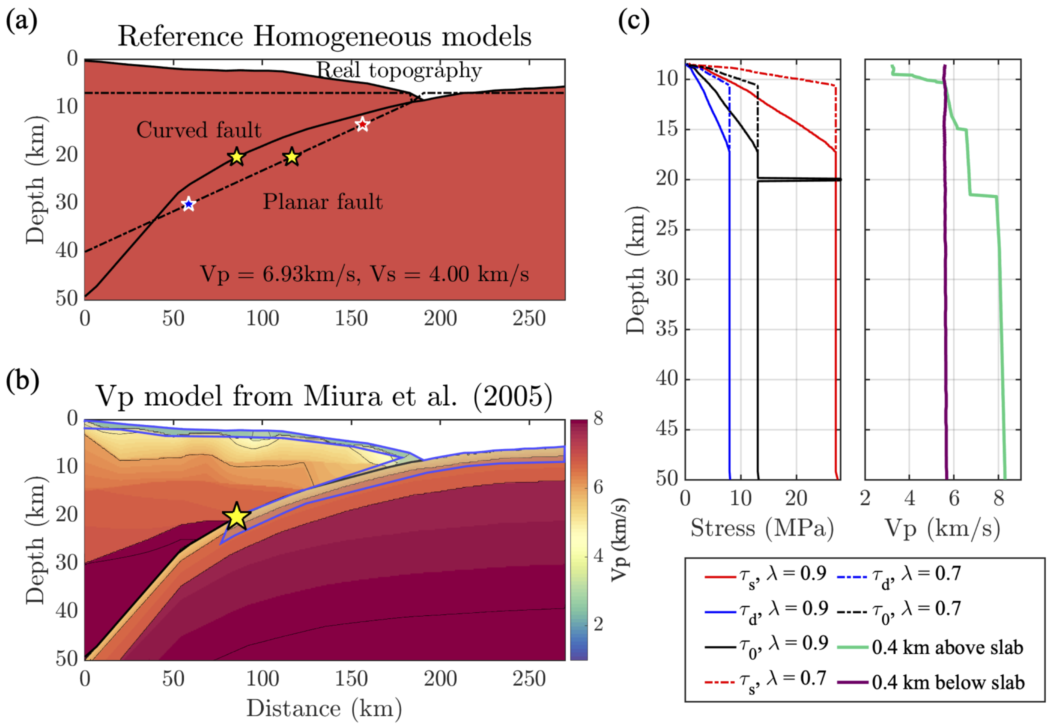

Figure 1. Model setting. (a) Homogeneous settings: flat half-space with planar slab/fault geometry and flat topography (dashed lines), a half-space with realistic slab geometry and seafloor topography (solid lines, referred to later as REF), hypocentral locations (yellow for the large ruptures, red and blue for the partial ruptures). (b) Heterogeneous half-space with realistic seafloor topography and P-wave velocity structure from Miura et al. (2005). (c) Fault properties: static strength levels τ_s (red), dynamic strength levels τ_d (blue), pre shear stress τ_0 (black) with different values of pore pressure ratio λ of 0.7 (dashed lines) and 0.9 (solid lines), P-wave velocity across 2 profiles projected at 400-m above (green) and 400-m below the plate interface (purple).

ping fault (11.8° degrees, Fig. 1a) to a heterogeneous half-space with a realistic geometry and a regional V_P structure from Miura et al. (2005) (Fig. 1b) . The elastic structure is observed to vary considerably along the dip of the megathrust, especially V_P in the upper plate (Sallarès & Ranero, 2019). Another aspect of the structure complexity is the presence of soft, highly compliant sediments in the accretionary wedge (Von Huene et al. (2009), and references herein). Here, we describe the megathrust fault zone into two canonical fault zone structures: 1) the updip fault zone has low-velocity properties, high V_P/V_S ratio, and wide damaged zone, and 2) the downdip fault structure has a sharp contrast in material properties across the fault.

In the updip region (upper 20 km), we concentrate our efforts on generating a realistic V_S structure. The compilation of V_P/V_S ratio values provided by Brocher (2005) suggests that low V_P materials have high V_P/V_S ratios. In light of this, we discuss three regions of possibly elevated V_P/V_S ratios. The first region is the subduction channel, a thin upper layer of the downgoing slab that is composed of fluid-rich seafloor sediments (Naif et al., 2015; Saffer & Tobin, 2011; Zhu et al., 2020) and hydrated minerals in a mafic fractured crust (Shelly et al., 2006; Bostock, 2013; Nishimura et al., 2019; Pimienta et al., 2018). The second region is the slope apron, a thin layer of the seafloor sediments atop the wedge that is best accessed by offshore drilling and active seismic surveys (Peacock et al., 2010; Tsuji et al., 2011; Fujie et al., 2013; Zhu et al., 2020). The third region we consider is the frontal prism that is also expected to drag high V_P/V_S ratio sediments (Saffer & Tobin, 2011; Fujie et al., 2013; Nakamura et al., 2014). Due to the range of V_P/V_S values found in the literature, we vary the ratios between $\sqrt{3}$ ~1.73, 1.83, 1.94, 2.04, 2.14, 2.24, 2.35, and 2.45 in the three specific regions discussed above (Fig. S1). Although higher values have been reported in seafloor sediment layers (Zhu et al., 2020), these are likely too thin to be resolved by our numerical exercise.

In the downdip region (between 20 and 50 km depth), we focus our attention on material contrasts at the plate interface. Although the downgoing oceanic plate is denser than the overriding plate, a several kilometer thin layer of the oceanic crust is known to have low seismic velocities. It is present in most subduction zones and referred to as a Low Velocity Zone (LVZ). To confirm this common feature of subduction zones, we compile the range of V_P in the LVZ and across the fault in the upper plate in Supplementary Materials Table S1.

Finally, we embed the realistic structure in a homogeneous half-space and generate a larger simulation domain to avoid artifacts in the absorbing boundary conditions. We impose a 5-km smoothing operator to taper off velocity changes between the high-resolution model and the homogeneous half-space (Supporting Information Figure S2). Finally, we also solve the problem of the buried curved fault in a homogeneous full-space as a benchmark case.

2.2 Modeling the dynamic rupture

The other ingredients necessary to model earthquake ruptures are fault properties such as the stress field, the pore pressure, and the frictional conditions (Fig. 1c). We explore several frictional conditions. In most models, we apply linear slip weakening on the entire fault. We test for slip-neutral and slip-strengthening conditions in the upper ~ 10 km of the along-dip direction, in a zone of low-grade metamorphism where neutrally stable conditions are expected to occur (Huang et al., 2012; Kozdon et al., 2013; Noda & Lapusta, 2013; Lotto et al., 2017, 2018). We also test the lab-based frictional constitutive relation proposed by Murphy et al. (2018). In addition to increasing the V_P/V_S ratio, the fluid content also affects the stress fields by reducing overburden lithostatic pressure σ_L with pore fluid pressure p. We use the pore pressure ratio λ defined in Hubbert and Rubey (1959) to impose a pore pressure $p = \lambda\sigma_L$ as well as the effective normal stress $\bar{\sigma}_n = (1 - \lambda)\sigma_L$. Given the uncertainties in λ, we test two cases of $\lambda = 0.7$ and 0.9 and assume that the pore fluid pressure becomes lithostatic ($\lambda = 1$) when $\bar{\sigma}_n =$ 40 MPa (Fig. 1d). These conditions are similar to those discussed and imposed in previous studies (e.g., Rice, 1992; Saffer & Tobin, 2011; Murphy et al., 2018; Lotto et al., 2018). The earthquake rupture naturally evolves on the fault in response to an over-stressed nucleation patch (see Fig. 1c). A full description of all model parameters can be found in the supplementary materials (Texts S1-S4). We use the SEM2DPACK software (`http://www.sourceforge.net/projects/sem2d/`, last accessed on 08/30/2019) to simultaneously solve for both the dynamic slip on the fault and the wavefield in the elastic two-dimensional domain.

2.3 Parameterization of the source radiation

To understand the relative contributions between LF and HF seismic waves emitted by the rupture, we parameterize the spectrum of the local slip-rate function, which has only been qualitatively discussed in Ma and Hirakawa (2013) and Galvez et al. (2014). In this study, we systematically measure and compare the along dip spectral variations in two ways.

The first way is to fit the Fourier amplitude spectrum of the local slip-rate function with a model that is flat at low frequencies and has a power-law decay at high frequencies (i.e., a pulse of finite width). We apply a model commonly used in source seismology $1/(1+(f/f_c)^n)$, where f_c and n are the corner frequency and spectral falloff rate, respectively. The spectral shape was designed to fit the far-field P-wave pulse shape that can be emitted by a circular crack rupture with uniform stress drop and elliptical slip distribution (Eshelby, 1957; Brune, 1970; Madariaga, 1976). It is common to perform spectral fitting over the spectrum of the far-field body-wave pulse of the entire event (Abercrombie & Rice, 2005; Allmann & Shearer, 2009; Trugman & Shearer, 2017; W. Wang & Shearer, 2019). While it is not an appropriate model for asymmetric surface-rupturing events, we simply use this spectral shape as a characterization of the spectral content. We use a non-linear least square solver to find f_c and n from fitting the $\log_{10}$ of the amplitude spectra of the local slip-rate functions interpolated on a logspace frequency vector, a strategy similar to other observational studies (see Shearer et al. (2019) for a recent review). The corner frequency f_c is inversely proportional to the pulse duration, which is also referred to as "rise time" in the kinematic representation of the source function. The spectral falloff rate n describes how fast the high-frequency component decays in amplitude. The combination of both parameters can help quantify the relative portions of LF and HF seismic radiation. They tradeoff each others during the spectral fit (Denolle & Shearer, 2016; Trugman & Shearer, 2017): larger f_c and smaller n correspond to relatively more HF radiation, while smaller f_c and larger n correspond to relatively more LF radiation.

The second measure of relative contribution in frequency content is an estimate of the seismic power generated by the local slip-acceleration function. We estimate the power by bandpassing (Butterworth, 4 corners, zero phase) and integrate the time series of local slip-acceleration functions in two frequency bands below the resolvable frequency: for partial rupture in the homogeneous medium (section 3.1), LF 0.001-0.05 Hz and HF 0.05 - 2 Hz; for full rupture (section 3.2), LF 0.001-0.06 Hz and HF 0.06 - 0.3 Hz. Details about the frequency resolution are included in the Supporting Information (Text S4). We then use the ratio of the HF and LF seismic powers (HF/LF power ratio) as a metric of relative contributions.

3 Results from dynamic rupture simulation of megathrust earthquakes

3.1 Cases of partial ruptures

We start by inquiring whether the model set up can reproduce the differences in pulse width and fall-off rate that have been inferred from observations of moderate-size subduction-zone events (Houston, 2001; Ye et al., 2016). We model two small ruptures in a simple structure of a planar fault and flat free surface (Fig. 1a). We impose pre-stress conditions to constrain the ruptures length but keep all other parameters equal for both simulations (Supporting Information Fig. S3). With this in mind, any difference in rupture style may be attributed to the depth (distance from the free surface) at which the rupture occurs. The shallow rupture reaches the trench and interacts with the scattered wavefields. This is not the case for the deep source as the rupture ends before the arrival of free-surface reflections; the deep source is effectively in a full-space. The simulations show that the shallow rupture ends up being about twice as large as the deep rupture (i.e., moment density released, Fig. 2a).

Next, we fit the overall moment-density-rate function with the spectral model within the resolvable frequency band below 2 Hz (Fig. 2c). This is in practice very similar to the source spectral studies that explore source parameters such as stress drop and radiated energy (e.g., Abercrombie & Rice, 2005; Baltay et al., 2014; Denolle & Shearer, 2016; Trugman & Shearer, 2017). The spectral analysis shows that the source spectrum of the shallow earthquake has lower $f_c = 0.16$ and higher $n = 2.25$ than the deep earthquake with $f_c = 0.19$ and $n = 2.04$ (Fig. 2c). f_c is expected to be lower given that the shallow rupture lasts longer and that the overall moment is greater. The stress drop is the same for both events by the construction of this dynamic model. The difference

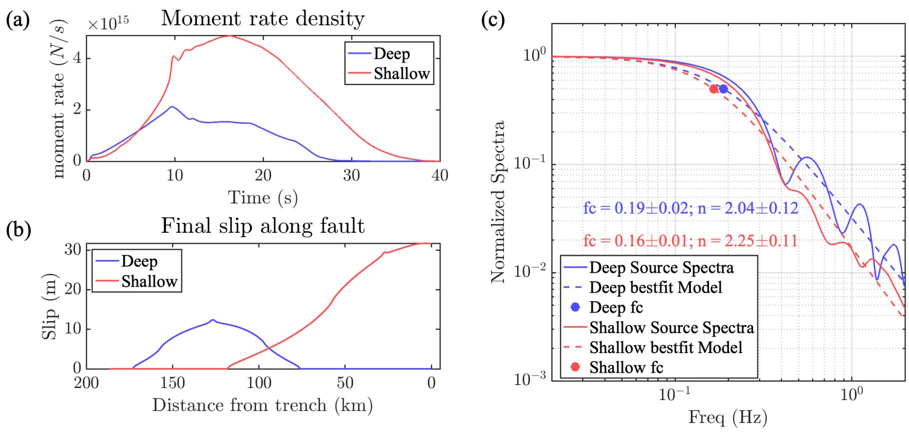

Figure 2. Simulation results of the two small earthquakes at different depths (Red: shallow; Blue: deep): (a) Slip-rate function averaged over the entire fault; (b) Final slip distribution on fault; (c) Amplitude-normalized source spectra of the two earthquakes (solid lines) as well as their corresponding best-fitted spectral models (dashed lines). Dots indicate the values of corner frequency f_c.

in corner frequency and moment does not follow the usual moment duration scaling expected for self-similar ruptures ($M_0 \sim T^3$), which probably stems from the difference between two-dimensional (2D) and three-dimensional (3D) models and because the shallow rupture does not have the same slip-profile as the deep rupture (Fig. 2b).

We also calculate the ratio of seismic power in a LF frequency band (here 0.001 - 0.05 Hz, well below the event corner frequencies) and a HF frequency band (here 0.05 - 2 Hz), as described above. The corresponding HF/LF ratio of shallow rupture is 0.771 while the ones for the deep rupture is 1.024, meaning that the shallow rupture is more depleted in HF than the deep rupture.

3.2 Cases of full ruptures

Our simulations in the half-space are typical to 2D models of dynamic ruptures (Huang et al., 2012; Kozdon et al., 2013; Lotto et al., 2017; Ramos & Huang, 2019). All simulated ruptures reach the trench, last about 60 seconds, and their final slip increases from small downdip to large updip. Examples of the space-time evolution of the ruptures are shown in Figure 3a. The rupture first propagates bilaterally from its nucleation patch. The updip rupture hits the trench with a high slip-rate and a weak re-rupture front propagates back downdip. The downdip rupture propagates with a constant rupture velocity and dies at the end of the fault. The slip profiles along dip (Fig. 4) are similar to the one inferred for the M9.0 2011 Tohoku-oki earthquake (Ide et al., 2011; Simons et al., 2011; K. Wang et al., 2018).

By comparison, the simulation that ran in the homogeneous full-space model presents a symmetric rupture behavior at the updip and downdip propagating fronts. There is only a slight difference due to the initial stress distribution (Fig. 3a and Fig. 4b). We refer to the Supporting Information 2 for detailed results of each individual model and summarize here their general patterns. To explore the depth-varying properties, we select one individual slip-rate function per 10-km segment, and discuss the segment-averages, which do not affect our conclusions, in Supporting Information (Fig. S4).

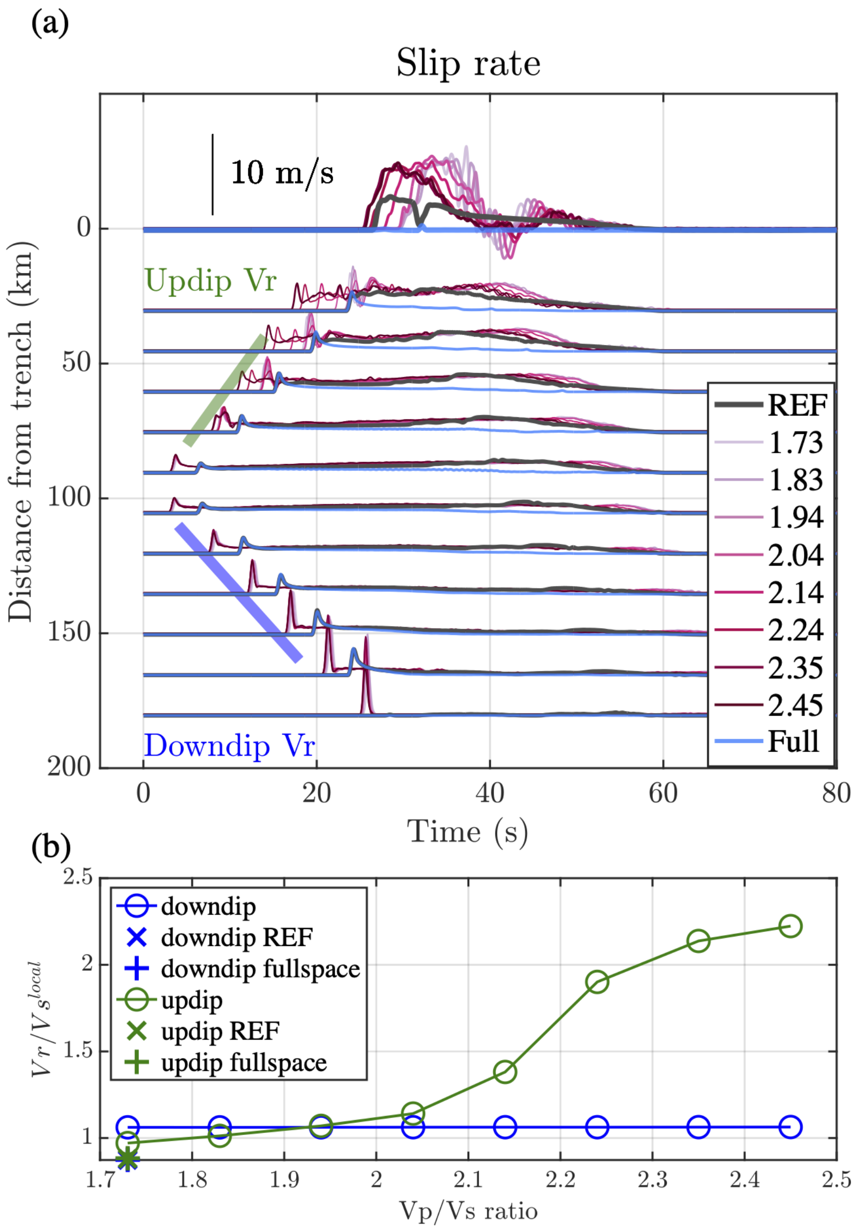

Figure 3. Comparisons of simulation results with $\lambda = 0.9$ from different values of V_P/V_S ratio under model settings (Fig. 1b) and homogeneous models: REF model with real topography in Figure 1a (dark gray) and full-space model (light blue). (a) Space-time slip-rate evolution: green and blue lines crudely mark the updip and downdip rupture front. (b) Rupture speeds of updip (in green, 40 km to 80 km from the trench) and downdip (in blue, 110 km to 160 km from the trench) propagation for each model.

We first perform the spectral fitting at each segment. We find that all models that have a free surface present similar variations of the spectral properties along dip, and therefore with depth (Fig. 5a and Fig. S4). The spectral falloff rate n generally decreases

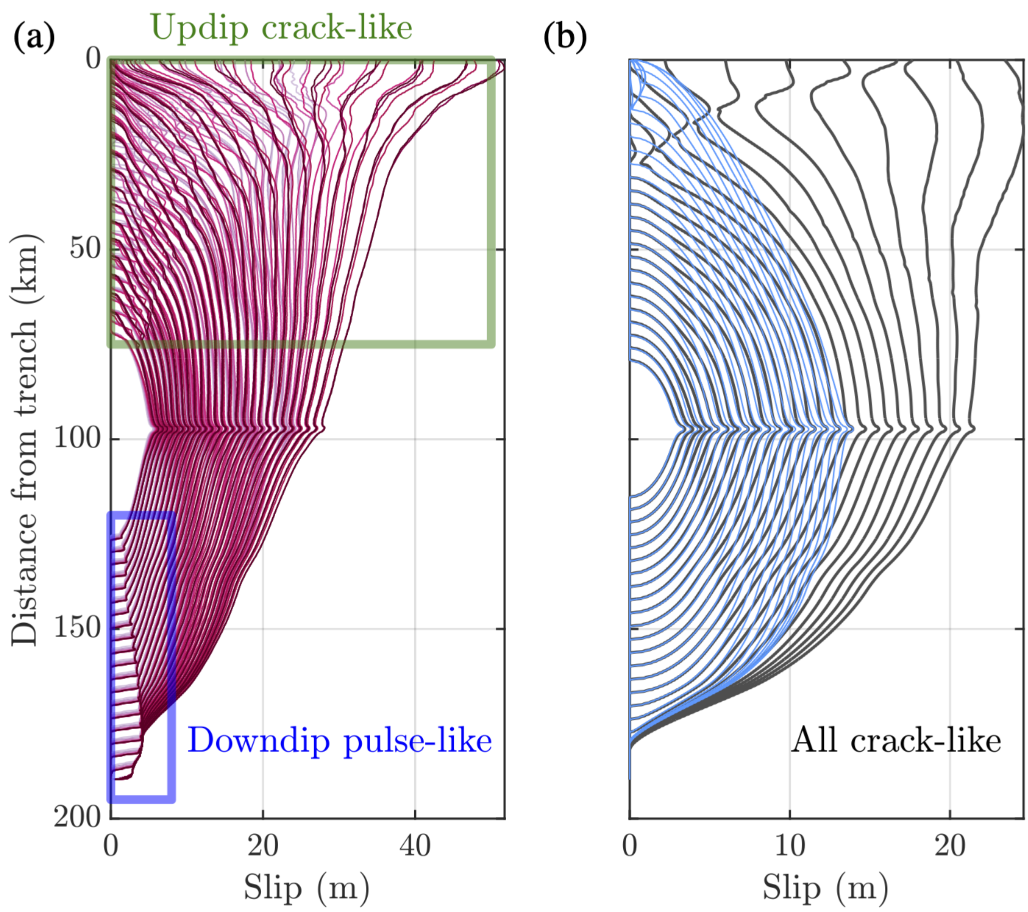

Figure 4. Snapshots of slip distribution from (a) models with heterogeneous velocity structures and different V_P/V_S ratios; (b) homogeneous models in half-space with real topography (dark gray) and in full-space (blue). Slip contours from every second between 10 to 35 s are plotted.

with depth: it is about 1.8 - 2.0 (model median) on the shallow segment from 0 - 20 km, and 0.8 - 1.0 (model median) on the deep segment.

Second, we calculate the power ratio of slip accelerations in the HF (0.06 - 0.3 Hz) and LF (0.001 - 0.06 Hz) bands. The central frequency 0.06 Hz is arbitrarily chosen in the middle within the resolvable frequency band, but it does not affect the results. We choose slip acceleration as the ground motion unit because far-field velocity seismograms, which are commonly used for teleseismic P-wave backprojection studies (Fukahata et al., 2014; Yin & Denolle, 2019), are proportional to moment accelerations. Here again, we find a clear pattern that the HF/LF power ratio increases with depth along dip for all those half-space models (Fig. 5b).

In all models with the free surface, both measures of relative frequency content of the local slip rate functions vary systematically with depth. This is not the case for the full-space model: both the spectral falloff rate n and the HF/LF ratio remain constant (Fig. 5). This suggests that the free surface effects are sufficient to explain the frequency-depth radiation in megathrust earthquakes.

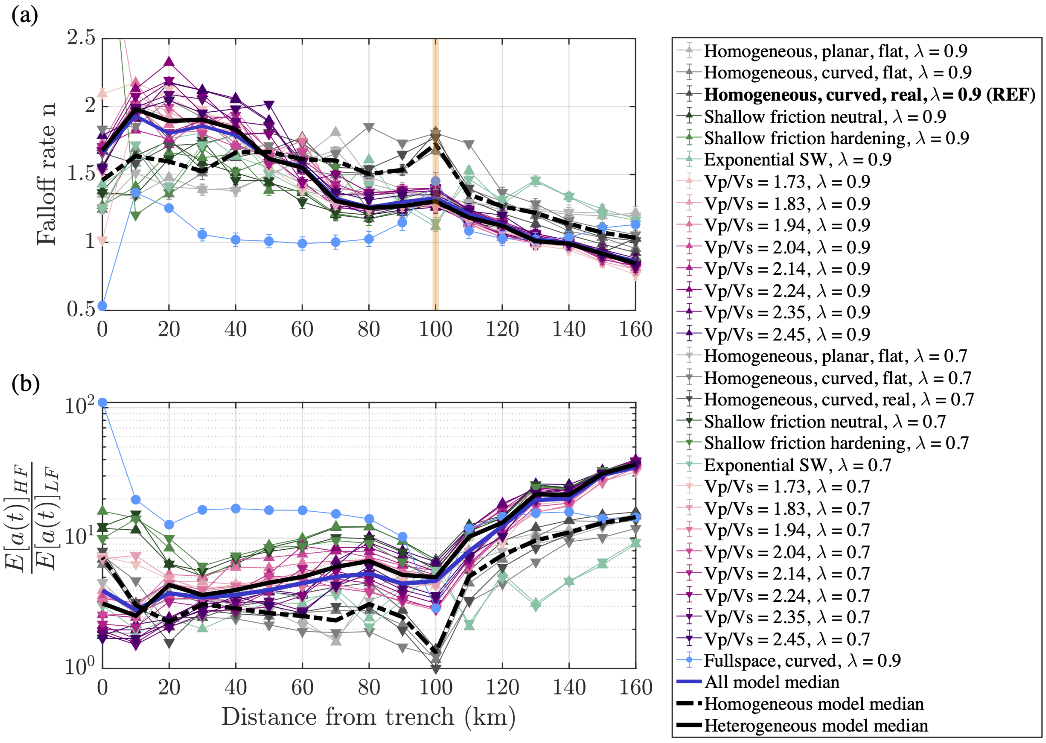

Figure 5. (a) Best-fitted spectral falloff rate n along dip from the simulated megathrust earthquake with different model settings. (b) The power ratio of high frequency (HF) 0.06 - 0.3 Hz and low frequency (LF) 0.001 - 0.06 Hz slip acceleration along dip. Colored lines refer to different models. The yellow bar indicate the location of rupture nucleation.

4 Discussion

This study focuses on the effects of realistic Earth structure on the dynamic rupture behavior of megathrust earthquakes. While we tested a particular subduction zone of the active margin in Northeastern Japan (Miura et al., 2005), the overall structure exists in many other subduction zones (Table S1). Three specific features in the structure appeared to play roles in explaining the depth-frequency relation of megathrust earthquakes (Fig. 6): 1) the free surface in the near-source region, 2) the highly compliant wedge updip, and 3) the low-velocity zone downdip below the plate interface downdip. The free surface effects are the dominant factor, but variations in compliance also enhance the radiation contrast. We illustrate this in Figure 6. Next, we discuss the rupture behavior and further argue that realistic structure is necessary for better seismic and tsunami hazard assessment.

4.1 Updip rupture: large and fast crack rupture to the trench

The rupture accelerates updip and is characterized by a crack-like mode (Fig. 4): rupture velocities are higher than typically observed (Chounet et al., 2018) and greater than the surrounding V_S, and slip continues until the end of rupture. Our simulations shed light on two major factors that control this updip behavior: the free surface and the shallow compliant fault zone.

Previous studies have shown that the free surface can significantly change the normal stress during rupture, due to waves reflecting at the free surface and traveling back

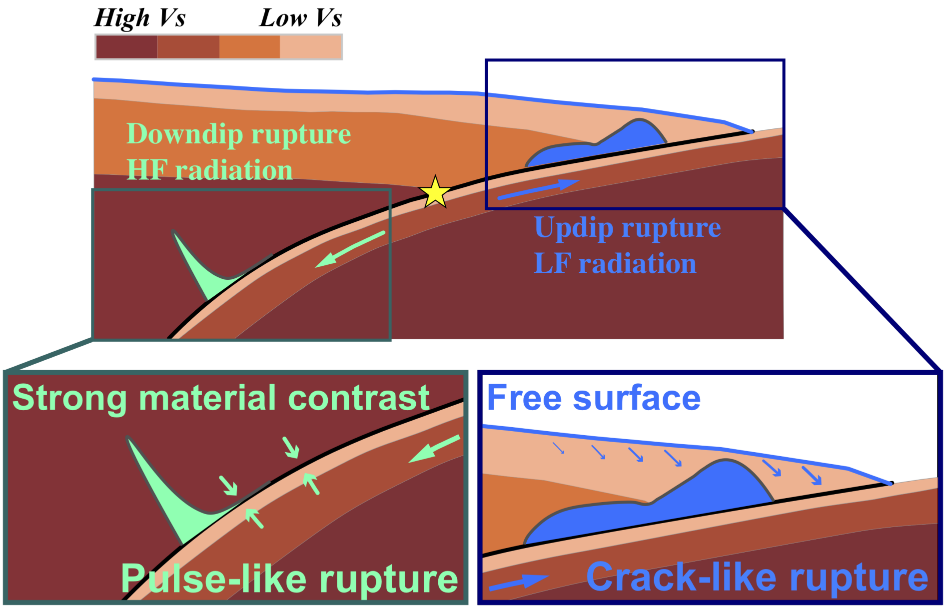

Figure 6. Cartoon of the effects of the free surface and material contrasts on the dynamic rupture behavior. In the updip region, the free surface leads to crack-like rupture and enhanced low frequency radiation. In the downdip region, the strong material contrast that occurs at the top of the Low Velocity Zone (LVZ) favors pulse-like rupture and enhanced high frequency seismic radiation.

to the fault (Brune, 1996; Nielsen, 1998; Oglesby et al., 1998, 2000; Y. Wang et al., 2019; Tal et al., 2020). Our simulation results are no different: clear surface-reflected phases cause the prolonged and persistent slip in the updip portion (Supporting Information 2). Free surface effects also induce acceleration of rupture propagation with speeds that are supershear, which is also seen in other tectonic regimes such as strike slip earthquakes (Kaneko & Lapusta, 2010).

On the hanging-wall side, the highly compliant structure in the shallow megathrust acts as a seismic waveguide. The upper plate low-velocity sediments can trap seismic waves, amplify their amplitudes and extend their duration. This is similar to how seismic waves get amplified in sedimentary basins (Campillo et al., 1989). Despite differences in model settings, all simulations show that the direct phase emitted at the rupture front, free-surface reflections, and other wedge captured and scattered waves interfere together to energize rupture and slip. In our simulations, these normal stress changes and fault-parallel slip are so extreme, with peak slip rates on the order of 10 m/s, that some models with standard V_P/V_S ratios predict co-seismic backslip (Fig. 3a). In simulations with higher V_P/V_S ratios, it is possible that much lower V_S delays the propagation of scattered waves in a way that limits their constructive interference back to the fault. Regardless, such extreme values of slip rates generate large dynamic stresses that can cause inelastic failure (Ma & Hirakawa, 2013; Ma & Nie, 2019), wedge flapping (Brune, 1996; Gabuchian et al., 2017), and may be the cause for the suggested dynamic overshoot during the M9.0 2011 Tohoku-Oki earthquake (Ide et al., 2011).

On the foot-wall side, the downgoing plate is fractured and hydrated with low velocities and elevated V_P/V_S ratios. All together, the structure is similar to that observed in observed crustal damage zones (Ben-Zion & Sammis, 2003). Harris and Day (1997) suggested that the low-velocity structure around the fault can perturb the rupture speed and slip-velocity pulse shape. Such low-velocity structure has dramatic effects on rupture propagation and termination such as multiple slip pulses, supershear rupture velocity and rotation of background stress (Ampuero & Ben-Zion, 2008; Huang et al., 2014; Huang, 2018).

In the homogeneous case with a uniform V_P/V_S ratio of $\sqrt{3}$ and realistic fault and seafloor geometry (REF model in Fig. 5 and Fig. 7), the rupture velocity for both up and down dip rupture has a typical value of $0.87V_S$. In structures that have realistic V_P/V_S ratios, the updip rupture velocity becomes greater than the local V_S. This is typical for 2D elastic models of subduction zone earthquakes (Lotto et al., 2018) and for rupture propagation in damaged fault zones (Huang et al., 2014; Weng et al., 2016; Huang et al., 2016).

4.2 Downdip rupture: pulse-like rupture along the LVZ

As the rupture propagates to the downdip region, the impact from free surface reflections can be neglected as the rupture heals before waves travel back to the fault. All models present a sharp rupture front (Fig. 3a). For the homogeneous models, the slip-rate functions have typical decays and long tails (Kostrov, 1964). For the heterogeneous models, the slip-rate functions are characterized by a shortening of the slip pulse (stronger healing) with depth/along dip or distance from the hypocenter. In both situations, our quantification on the spectrum shows that the HF energy is dominated due to the sharp slip-rate function shape.

The evolution of short and sharp slip pulses in the heterogeneous models can be explained by the material contrast at the plate interface downdip of the hypocenter. Shlomai and Fineberg (2016) performed and analyzed lab experiments to shear two materials with different properties. With an in-plane shear of the two blocks (relevant to this setting), they found that such bimaterial interface can host both rupture modes: one self-healing slip pulse that moves in one direction of rupture and one slip crack that propagates in the opposite direction. The experimental configuration is similar to that the subduction zones downdip of the seismogenic zone with the contact between the LVZ and the overhanging upper mantle material. As the rupture propagates downdip, in the moving direction of the compliant oceanic plate, the slip-rate functions are short and sharp pulses (Fig. 3a), and the corresponding downdip rupture speed V_r is close to the local V_S of the oceanic crust near the slab (Fig. 3b).

4.3 Frequency-depth radiation of megathrust earthquakes

In this study, we have shown that all simulated earthquakes in half-spaces exhibit a common pattern that along-dip variations in spectral parameters and HF/LF ratios of the local slip-rate functions (Fig. 2, Figure 5 (a) and (b)), are consistent with the observed depth-frequency relation. By contrast, the benchmark full-space simulation is not. Therefore, the free surface effects are the leading factor in explaining the observed depth-frequency relation of megathrust earthquakes.

The cases of partial ruptures (Fig. 2) show that the shallow one is more depleted in high-frequency radiation than the deep one. Those patterns are consistent with the observed systematic variations of source parameters for small-to-moderate earthquakes at different depth (Houston, 2001; Ko & Kuo, 2016; Denolle & Shearer, 2016; Ye et al., 2016).

The cases of full ruptures also show that the deep portion of the rupture is enriched in high-frequency radiation compared to the shallow portion of the rupture. We bring attention to the backprojection results that have shown a depth-frequency relation during individual megathrust earthquakes (Lay et al., 2012; D. Wang & Mori, 2011; Sufri et al., 2012; Yao et al., 2013; Melgar et al., 2016; Yin et al., 2016, 2017, 2018). Fukahata et al. (2014) and Yin and Denolle (2019) show that the backprojection images are snapshots of a slip-rate map with an array-specific spatial smoothing. Therefore, the analysis of the slip-rate functions of our simulations can be directly related to the kinematic observations including both slip inversion and backprojection imaging. In this study, we find a systematic pattern that the updip region is characterized by a crack-like rupture mode while the downdip region is characterized by a pulse-like rupture mode. The quantification of slip-rate functions in the spectral domain (Figs. 5a and b) validates that the different rupture modes can explain the depth-frequency relation: i) in the updip region, the rupture radiates more efficiently LF seismic waves due to the effects of the complex structure on the earthquake dynamics, ii) in the downdip region, the rupture radiates more efficiently HF seismic waves due to the strong material contrast from LVZ and continental mantle.

Furthermore, we notice that the models that include realistic velocity structures (Fig. 5b) tend to present stronger contrast in the frequency content of the radiation as a function of depth, with larger differences in values of falloff rate n and HF/LF ratios. Therefore, the shallow compliant structures can be another specific factor to enhance the depth-varying frequency-dependence of seismic radiation.

4.4 Implications for tsunami and ground motion hazards

The megathrust earthquake simulations further show that using realistic structures is necessary for proper assessment of shaking and tsunami hazards (Fig. 7). The elastic properties in the homogeneous cases are greater than that in the heterogeneous cases, which results in greater moment for the reference case.

Our simulations indicate that the final slip distribution varies particularly with the model settings. The final moment magnitude of the homogeneous half-space models is larger than the heterogeneous models, probably in part due to the greater shear modulus at the shallow portion (Fig. 7a). However, the final slip is greatly amplified by the compliant structures near the trench (Fig.7b), which was also found in Lotto et al. (2018). The final fault-parallel slip near the trench directly impacts the tsunami height. We use a simple relation from Tanioka and Satake (1996) to estimate the initial height of the tsunami η_{ts} at the trench: $\eta_{ts} = u_y - m u_x$, where u_x, u_y and $m = -0.1$ are the horizontal displacement, vertical displacement, and the horizontal gradient of bathymetry at the trench in this setting, respectively. We find that $\eta_{ts} = 8.6$ m for the homogeneous half-space model (model REF), 11.0 m for the heterogeneous model with $V_P/V_S = \sqrt{3}$ and 11.3 m for the heterogeneous model with $V_P/V_S = 2.45$. This simple exercise confirms previous studies that the realistic velocity structure, especially the shallow V_S structure, needs to be represented for better estimation of the potential tsunami hazards (Lotto et al., 2018).

We also compare the ground motions that would be recorded at a station in the coastal region (Fig. 7c-d). The strong ground motions that are responsible for damaging urban infrastructure may arrive as distinct high-frequency bursts from the downdip of the megathrust (Kurahashi & Irikura, 2011; Asano & Iwata, 2012; Frankel, 2013). Moment-normalized velocity and acceleration seismograms produced by different models have relatively similar peak amplitudes. The earliest peak amplitudes of ground motions occur when ruptures hit the trench. However, the duration of strong shaking is much greater in realistic structures. We attribute this to resonances in the wedge (wave propagation effects) and not a source effect since the source duration is comparable (~ 60 s). Because strong ground motions are mainly governed by the downdip structure, we find that the presence of the LVZ naturally enhances the strong ground motions and the heterogeneous models tend to have about 3 times more HF/LF power ratio than the homogeneous models (Fig.5). Previous studies have illustrated the existence of distinct strong motion gen-

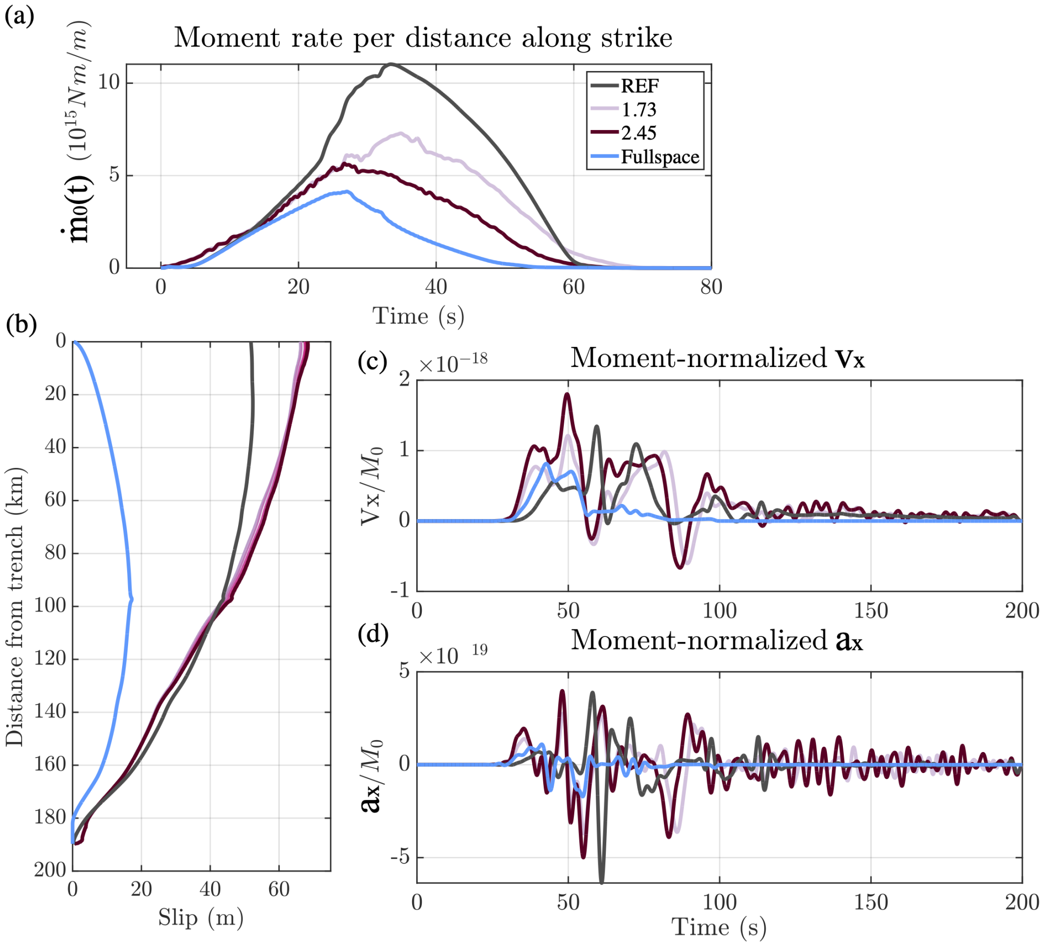

Figure 7. (a) The moment-rate density function of each model with different V_P/V_S ratios. (b) The final slip distribution along dip from different models. (c) Moment-normalized velocity seismograms (horizontal x direction) recorded by the far field station (location shown in Fig. S2b). (d) The corresponding moment-normalized acceleration seismograms (horizontal x direction) recorded by the same virtual station.

eration areas (SMGAs) (Kurahashi & Irikura, 2011; Asano & Iwata, 2012; Frankel, 2013). The SMGAs imply that there may be heterogeneity in the LVZ such that the spatial variations in elastic structure may control variations in slip-front healing (i.e. more or less healing of the slip pulse). This can also be modeled by heterogeneity in fault properties (Huang et al., 2012).

5 Conclusion

This study shows that realistic Earth structures, including the Earth surface, are necessary, and sufficient to explain the ubiquitous observations of depth variation in the radiation of subduction zone earthquakes. Sallarès and Ranero (2019) evoke that the increase in elastic properties with depth explains the increase in the dominant frequency of the seismic radiation. While this suggestion is plausible, the argument would pertain to all other tectonic regimes, which is not necessarily observed. Here, we argue that the dynamics of shallow rupture can predict these observations. The free surface effect is the first leading factor in explaining the depth-frequency relation. The second-order effect is the evolution of earthquake rupture in a structure that is typical of shallow subduction zones with a compliant wedge and a low-velocity zone atop the downgoing slab. The presence of anomalously low V_S, relative to V_P, also triggers a rupture behavior that further exaggerates the depth-dependence in the radiation frequency.

Our findings resonate with previous work that realistic structures are necessary to properly model tsunami and ground motion hazards in future subduction zone earthquakes (Lotto et al., 2018). Because tomographic models are likely better constrained than frictional properties at depth, our study promotes the use of tomographic images in dynamic rupture modeling and ground motion predictions. Our simulations do not include inelastic rheology that predicts greater tsunami hazards (Ma & Hirakawa, 2013; Ma & Nie, 2019), and are likely to affect on-fault rupture propagation and far-field radiation. More realistic Earth structure and material rheological properties are important research directions to better predict earthquake behavior, tsunami and ground motion hazards.

Acknowledgments

We sincerely thank Seiichi Miura at JAMSTEC (Japan Agency for Marine-Earth Science and Technology) for providing the velocity model of the Japan trench. We are grateful to Yihe Huang and Alice-Agnes Gabriel for constructive and productive discussions. We are grateful to the code developer of SEM2DPACK (available at `http://www.sourceforge.net/projects/sem2d/`) Jean-Paul Ampuero. All the down-sampled simulation results and relevant scripts have been uploaded to figshare (`https://figshare.com/projects/The_Earth_surface_controls_the_depth-dependent_seismic_radiation_of_megathrust_earthquakes/98360`) for purpose of result reproduction. This work is supported by the NSF (grants NSF CAREER EAR-1749556).

References

Abercrombie, R. E., & Rice, J. R. (2005). Can observations of earthquake scaling constrain slip weakening? *Geophysical Journal International*, *162*(2), 406–424. doi: 10.1111/j.1365-246X.2005.02579.x

Allmann, B. P., & Shearer, P. M. (2009). Global variations of stress drop for moderate to large earthquakes. *Journal of Geophysical Research: Solid Earth*, *114*(B1), B01310. doi: 10.1029/2008JB005821

Ampuero, J.-P., & Ben-Zion, Y. (2008). Cracks, pulses and macroscopic asymmetry of dynamic rupture on a bimaterial interface with velocity-weakening friction. *Geophysical Journal International*, *173*(2), 674–692. doi: 10.1111/j.1365-246X.2008.03736.x

Asano, K., & Iwata, T. (2012). Source model for strong ground motion generation in the frequency range 0.1–10 Hz during the 2011 Tohoku earthquake. *Earth, Planets and Space*, *64*(12), 6. doi: 10.5047/eps.2012.05.003

Baltay, A. S., Beroza, G. C., & Ide, S. (2014). Radiated Energy of Great Earthquakes from Teleseismic Empirical Green's Function Deconvolution. *Pure and Applied Geophysics*, *171*(10), 2841–2862. doi: 10.1007/s00024-014-0804-0

Ben-Zion, Y., & Sammis, C. G. (2003). Characterization of fault zones. *Pure and applied geophysics*, *160*(3), 677–715.

Bostock, M. G. (2013). The Moho in subduction zones. *Tectonophysics*, *609*, 547–557. doi: 10.1016/j.tecto.2012.07.007

Brocher, T. M. (2005, 12). Empirical Relations between Elastic Wavespeeds and Density in the Earth's Crust. *Bulletin of the Seismological Society of America*, *95*(6), 2081-2092. doi: 10.1785/0120050077

Brune, J. N. (1970). Tectonic stress and the spectra of seismic shear waves from earthquakes. *Journal of Geophysical Research*, *75*(26), 4997–5009. doi: 10.1029/JB075i026p04997

Brune, J. N. (1996). Particle motions in a physical model of shallow angle thrust faulting. *Proceedings of the Indian Academy of Sciences - Earth and Planetary Sciences*, *105*(2), 197. doi: 10.1007/BF02876014

Campillo, M., Gariel, J., Aki, K., & Sanchez-Sesma, F. (1989). Destructive strong ground motion in mexico city: Source, path, and site effects during great 1985 michoacán earthquake. *Bulletin of the Seismological Society of America*, *79*(6), 1718–1735.

Chounet, A., Vallée, M., Causse, M., & Courboulex, F. (2018). Global catalog of earthquake rupture velocities shows anticorrelation between stress drop and rupture velocity. *Tectonophysics*, *733*, 148–158. doi: 10.1016/j.tecto.2017.11.005

Denolle, M. A., & Shearer, P. M. (2016). New perspectives on self-similarity for shallow thrust earthquakes. *Journal of Geophysical Research: Solid Earth*, *121*(9), 2016JB013105. doi: 10.1002/2016JB013105

Eshelby, J. D. (1957). The determination of the elastic field of an ellipsoidal inclusion, and related problems. , *241*, 376–396.

Frankel, A. (2013). Rupture History of the 2011 M 9 Tohoku Japan Earthquake Determined from Strong-Motion and High-Rate GPS Recordings: Subevents Radiating Energy in Different Frequency BandsRupture History of the 2011 M 9 Tohoku Earthquake from Strong-Motion and High-Rate GPS Recordings. *Bulletin of the Seismological Society of America*, *103*(2B), 1290–1306. doi: 10.1785/0120120148

Fujie, G., Kodaira, S., Yamashita, M., Sato, T., Takahashi, T., & Takahashi, N. (2013). Systematic changes in the incoming plate structure at the Kuril trench. *Geophysical Research Letters*, *40*(1), 88–93. doi: https://doi.org/10.1029/2012GL054340

Fukahata, Y., Yagi, Y., & Rivera, L. (2014). Theoretical relationship between back-projection imaging and classical linear inverse solutions. *Geophysical Journal International*, *196*(1), 552–559.

Gabuchian, V., Rosakis, A. J., Bhat, H. S., Madariaga, R., & Kanamori, H. (2017). Experimental evidence that thrust earthquake ruptures might open faults. *Nature*, *545*(7654), 336–339.

Galvez, P., Ampuero, J.-P., Dalguer, L. A., Somala, S. N., & Nissen-Meyer, T. (2014). Dynamic earthquake rupture modelled with an unstructured 3-D spectral element method applied to the 2011 M9 Tohoku earthquake. *Geophysical Journal International*, *198*(2), 1222–1240. doi: 10.1093/gji/ggu203

Guo, Y., Koketsu, K., & Miyake, H. (2016). Propagation mechanism of long-period ground motions for offshore earthquakes along the nankai trough: Effects of the accretionary wedge. *Bulletin of the Seismological Society of America*, *106*(3), 1176–1197.

Harris, R. A., & Day, S. M. (1997). Effects of a low-velocity zone on a dynamic rupture. *Bulletin of the Seismological Society of America*, *87*(5), 1267–1280.

Houston, H. (2001). Influence of depth, focal mechanism, and tectonic setting on the shape and duration of earthquake source time functions. *Journal of Geophysical Research: Solid Earth*, *106*(B6), 11137–11150. doi: 10.1029/2000JB900468

Huang, Y. (2018). Earthquake Rupture in Fault Zones With Along-Strike Material Heterogeneity. *Journal of Geophysical Research: Solid Earth*, *123*(11), 9884–9898. doi: https://doi.org/10.1029/2018JB016354

Huang, Y., Ampuero, J.-P., & Helmberger, D. V. (2014). Earthquake ruptures modulated by waves in damaged fault zones. *Journal of Geophysical Research: Solid Earth*, *119*(4), 3133–3154. doi: 10.1002/2013JB010724

Huang, Y., Ampuero, J.-P., & Helmberger, D. V. (2016). The potential for supershear earthquakes in damaged fault zones–theory and observations. *Earth and Planetary Science Letters*, *433*, 109–115.

Huang, Y., Meng, L., & Ampuero, J.-P. (2012). A dynamic model of the frequency-dependent rupture process of the 2011 Tohoku-Oki earthquake. *Earth, Planets and Space*, *64*(12), 1. doi: 10.5047/eps.2012.05.011

Hubbert, M. K., & Rubey, W. W. (1959). Role of fluid pressure in mechanics of overthrust faulting: I. mechanics of fluid-filled porous solids and its application to overthrust faulting. *GSA Bulletin*, *70*(2), 115–166. doi: 10.1130/0016-7606(1959)70[115:ROFPIM]2.0.CO;2

Ide, S., Baltay, A., & Beroza, G. C. (2011). Shallow dynamic overshoot and energetic deep rupture in the 2011 mw 9.0 tohoku-oki earthquake. *Science*, *332*(6036), 1426–1429.

Ishii, M., Shearer, P. M., Houston, H., & Vidale, J. E. (2005). Extent, duration and speed of the 2004 Sumatra–Andaman earthquake imaged by the Hi-Net array. *Nature*, *435*(7044), 933. doi: 10.1038/nature03675

Kaneko, Y., & Lapusta, N. (2010). Supershear transition due to a free surface in 3-D simulations of spontaneous dynamic rupture on vertical strike-slip faults. *Tectonophysics*, *493*(3), 272–284. doi: 10.1016/j.tecto.2010.06.015

Kiser, E., Ishii, M., Langmuir, C. H., Shearer, P. M., & Hirose, H. (2011). Insights into the mechanism of intermediate-depth earthquakes from source properties as imaged by back projection of multiple seismic phases. *Journal of Geophysical Research: Solid Earth*, *116*(B6), B06310. doi: 10.1029/2010JB007831

Ko, J. Y.-T., & Kuo, B.-Y. (2016). Low radiation efficiency of the intermediate-depth earthquakes in the Japan subduction zone. *Geophysical Research Letters*, *43*(22), 2016GL070993. doi: 10.1002/2016GL070993

Kostrov, B. V. (1964). Selfsimilar problems of propagation of shear cracks. *Journal of Applied Mathematics and Mechanics*, *28*(5), 1077–1087. doi: 10.1016/0021-8928(64)90010-3

Kozdon, J. E., Dunham, E. M., & Nordström, J. (2013). Simulation of Dynamic Earthquake Ruptures in Complex Geometries Using High-Order Finite Difference Methods. *Journal of Scientific Computing*, *55*(1), 92–124. doi: 10.1007/s10915-012-9624-5

Kurahashi, S., & Irikura, K. (2011). Source model for generating strong ground motions during the 2011 off the Pacific coast of Tohoku Earthquake. *Earth, Planets and Space*, *63*(7), 11. doi: 10.5047/eps.2011.06.044

Lay, T., Kanamori, H., Ammon, C. J., Koper, K. D., Hutko, A. R., Ye, L., … Rushing, T. M. (2012). Depth-varying rupture properties of subduction zone megathrust faults. *Journal of Geophysical Research: Solid Earth*, *117*(B4), B04311. doi: 10.1029/2011JB009133

Lotto, G. C., Dunham, E. M., Jeppson, T. N., & Tobin, H. J. (2017). The effect of compliant prisms on subduction zone earthquakes and tsunamis. *Earth and Planetary Science Letters*, *458*, 213–222. doi: 10.1016/j.epsl.2016.10.050

Lotto, G. C., Jeppson, T. N., & Dunham, E. M. (2018). Fully Coupled Simulations of Megathrust Earthquakes and Tsunamis in the Japan Trench, Nankai Trough, and Cascadia Subduction Zone. *Pure and Applied Geophysics*. doi: 10.1007/s00024-018-1990-y

Ma, S., & Beroza, G. C. (2008). Rupture Dynamics on a Bimaterial Interface for Dipping FaultsRupture Dynamics on a Bimaterial Interface for Dipping Faults. *Bulletin of the Seismological Society of America*, *98*(4), 1642–1658. doi: 10.1785/0120070201

Ma, S., & Hirakawa, E. T. (2013). Dynamic wedge failure reveals anomalous energy radiation of shallow subduction earthquakes. *Earth and Planetary Science Letters*, *375*, 113–122. doi: 10.1016/j.epsl.2013.05.016

Ma, S., & Nie, S. (2019). Dynamic wedge failure and along-arc variations of tsunamigenesis in the japan trench margin. *Geophysical Research Letters*, *46*(15), 8782-8790. doi: 10.1029/2019GL083148

Madariaga, R. (1976). Dynamics of an expanding circular fault. *Bulletin of the Seis-*

mological Society of America, *66*(3), 639–666.

Melgar, D., Fan, W., Riquelme, S., Geng, J., Liang, C., Fuentes, M., … Fielding, E. J. (2016). Slip segmentation and slow rupture to the trench during the 2015, Mw8.3 Illapel, Chile earthquake. *Geophysical Research Letters*, *43*(3), 2015GL067369. doi: 10.1002/2015GL067369

Miura, S., Takahashi, N., Nakanishi, A., Tsuru, T., Kodaira, S., & Kaneda, Y. (2005). Structural characteristics off Miyagi forearc region, the Japan Trench seismogenic zone, deduced from a wide-angle reflection and refraction study. *Tectonophysics*, *407*(3), 165–188. doi: 10.1016/j.tecto.2005.08.001

Murphy, S., Di Toro, G., Romano, F., Scala, A., Lorito, S., Spagnuolo, E., … Nielsen, S. (2018). Tsunamigenic earthquake simulations using experimentally derived friction laws. *Earth and Planetary Science Letters*, *486*, 155–165. doi: 10.1016/j.epsl.2018.01.011

Naif, S., Key, K., Constable, S., & Evans, R. L. (2015). Water-rich bending faults at the Middle America Trench. *Geochemistry, Geophysics, Geosystems*, *16*(8), 2582–2597. doi: 10.1002/2015GC005927

Nakamura, Y., Kodaira, S., Cook, B. J., Jeppson, T., Kasaya, T., Yamamoto, Y., … Fujie, G. (2014). Seismic imaging and velocity structure around the JFAST drill site in the Japan Trench: low V p, high V p/V s in the transparent frontal prism. *Earth, Planets and Space*, *66*(1), 121. doi: 10.1186/1880-5981-66-121

Nielsen, S. B. (1998). Free surface effects on the propagation of dynamic rupture. *Geophysical Research Letters*, *25*(1), 125–128. doi: 10.1029/97GL03445

Nishimura, K., Uehara, S., & Mizoguchi, K. (2019). An alternative origin of high vp/vs anomalies in slow slip regions: Experimental constraints from the elastic wave velocity evolution of highly fractured rock. *Journal of Geophysical Research: Solid Earth*, *124*(5), 5045–5059.

Noda, H., & Lapusta, N. (2013). Stable creeping fault segments can become destructive as a result of dynamic weakening. *Nature*, *493*(7433), 518–521. doi: 10.1038/nature11703

Oglesby, D. D., Archuleta, R. J., & Nielsen, S. B. (1998). Earthquakes on Dipping Faults: The Effects of Broken Symmetry. *Science*, *280*(5366), 1055–1059. doi: 10.1126/science.280.5366.1055

Oglesby, D. D., Archuleta, R. J., & Nielsen, S. B. (2000). Dynamics of dip-slip faulting: Explorations in two dimensions. *Journal of Geophysical Research: Solid Earth*, *105*(B6), 13643–13653.

Peacock, S., Westbrook, G. K., & Bais, G. (2010). S-wave velocities and anisotropy in sediments entering the Nankai subduction zone, offshore Japan. *Geophysical Journal International*, *180*(2), 743–758. doi: 10.1111/j.1365-246X.2009.04430.x

Pimienta, L., Schubnel, A., Violay, M., Fortin, J., Guéguen, Y., & Lyon-Caen, H. (2018). Anomalous vp/vs ratios at seismic frequencies might evidence highly damaged rocks in subduction zones. *Geophysical Research Letters*, *45*(22), 12,210-12,217. doi: https://doi.org/10.1029/2018GL080132

Ramos, M. D., & Huang, Y. (2019). How the Transition Region Along the Cascadia Megathrust Influences Coseismic Behavior: Insights From 2-D Dynamic Rupture Simulations. *Geophysical Research Letters*, *46*(4), 1973–1983. doi: 10.1029/2018GL080812

Rice, J. R. (1992). Chapter 20 Fault Stress States, Pore Pressure Distributions, and the Weakness of the San Andreas Fault. In B. Evans & T.-f. Wong (Eds.), *International Geophysics* (Vol. 51, pp. 475–503). Academic Press. doi: 10.1016/S0074-6142(08)62835-1

Saffer, D. M., & Tobin, H. J. (2011). Hydrogeology and mechanics of subduction zone forearcs: Fluid flow and pore pressure. *Annual Review of Earth and Planetary Sciences*, *39*, 157–186.

Sallarès, V., & Ranero, C. R. (2019). Upper-plate rigidity determines depth-varying rupture behaviour of megathrust earthquakes. *Nature*, *576*(7785). doi: 10.1038/s41586-019-1784-0

Scholz, C. H. (1998). Earthquakes and friction laws. *Nature*, *391*(6662), 37–42. doi: 10.1038/34097

Shearer, P. M., Abercrombie, R. E., Trugman, D. T., & Wang, W. (2019). Comparing egf methods for estimating corner frequency and stress drop from p wave spectra. *Journal of Geophysical Research: Solid Earth*, *124*(4), 3966–3986.

Shelly, D. R., Beroza, G. C., Zhang, H., Thurber, C. H., & Ide, S. (2006). High-resolution subduction zone seismicity and velocity structure beneath Ibaraki Prefecture, Japan. *Journal of Geophysical Research: Solid Earth*, *111*(B6). doi: 10.1029/2005JB004081

Shlomai, H., & Fineberg, J. (2016). The structure of slip-pulses and supershear ruptures driving slip in bimaterial friction. *Nature Communications*, *7*(1). doi: 10.1038/ncomms11787

Simons, M., Minson, S. E., Sladen, A., Ortega, F., Jiang, J., Owen, S. E., ... Webb, F. H. (2011). The 2011 Magnitude 9.0 Tohoku-Oki Earthquake: Mosaicking the Megathrust from Seconds to Centuries. *Science*, *332*(6036), 1421–1425. doi: 10.1126/science.1206731

Sufri, O., Koper, K. D., & Lay, T. (2012). Along-dip seismic radiation segmentation during the 2007 Mw 8.0 Pisco, Peru earthquake. *Geophysical Research Letters*, *39*(8), L08311. doi: 10.1029/2012GL051316

Tal, Y., Rubino, V., Rosakis, A. J., & Lapusta, N. (2020). Illuminating the physics of dynamic friction through laboratory earthquakes on thrust faults. *Proceedings of the National Academy of Sciences*, *117*(35), 21095–21100.

Tanioka, Y., & Satake, K. (1996). Tsunami generation by horizontal displacement of ocean bottom. *Geophysical Research Letters*, *23*(8), 861–864. doi: 10.1029/96GL00736

Trugman, D. T., & Shearer, P. M. (2017). Application of an improved spectral decomposition method to examine earthquake source scaling in Southern California. *Journal of Geophysical Research: Solid Earth*, *122*(4), 2890–2910. doi: https://doi.org/10.1002/2017JB013971

Tsuji, T., Dvorkin, J., Mavko, G., Nakata, N., Matsuoka, T., Nakanishi, A., ... Nishizawa, O. (2011). VP/VS ratio and shear-wave splitting in the Nankai Trough seismogenic zone: Insights into effective stress, pore pressure, and sediment consolidationTsuji et al.VP/VS ratio & S-wave splitting from OBS data. *Geophysics*, *76*(3), WA71–WA82. doi: 10.1190/1.3560018

Vallée, M. (2013). Source time function properties indicate a strain drop independent of earthquake depth and magnitude. *Nature Communications*, *4*, 2606. doi: 10.1038/ncomms3606

Von Huene, R., Ranero, C. R., & Scholl, D. W. (2009). Convergent margin structure in high-quality geophysical images and current kinematic and dynamic models. In *Subduction zone geodynamics* (pp. 137–157). Springer.

Wang, D., & Mori, J. (2011). Frequency-dependent energy radiation and fault coupling for the 2010 Mw8.8 Maule, Chile, and 2011 Mw9.0 Tohoku, Japan, earthquakes. *Geophysical Research Letters*, *38*(22). doi: 10.1029/2011GL049652

Wang, K., Sun, T., Brown, L., Hino, R., Tomita, F., Kido, M., ... Fujiwara, T. (2018). Learning from crustal deformation associated with the M9 2011 Tohoku-oki earthquake. *Geosphere*, *14*(2), 552–571. doi: 10.1130/GES01531.1

Wang, W., & Shearer, P. M. (2019). An improved method to determine coda-q, earthquake magnitude, and site amplification: Theory and application to southern california. *Journal of Geophysical Research: Solid Earth*, *124*(1), 578–598. doi: https://doi.org/10.1029/2018JB015961

Wang, Y., Day, S. M., & Denolle, M. A. (2019). Geometric Controls on Pulse-Like Rupture in a Dynamic Model of the 2015 Gorkha Earthquake.

Journal of Geophysical Research: Solid Earth, *124*(2), 1544–1568. doi: 10.1029/2018JB016602

Weng, H., Yang, H., Zhang, Z., & Chen, X. (2016). Earthquake rupture extents and coseismic slips promoted by damaged fault zones. *Journal of Geophysical Research: Solid Earth*, *121*(6), 4446–4457. doi: 10.1002/2015JB012713

Yao, H., Shearer, P. M., & Gerstoft, P. (2013). Compressive sensing of frequency-dependent seismic radiation from subduction zone megathrust ruptures. *Proceedings of the National Academy of Sciences*, *110*(12), 4512–4517. doi: 10.1073/pnas.1212790110

Ye, L., Lay, T., Kanamori, H., & Rivera, L. (2016). Rupture characteristics of major and great (mw 7.0) megathrust earthquakes from 1990 to 2015: 2. depth dependence. *Journal of Geophysical Research: Solid Earth*, *121*(2), 845–863.

Yin, J., & Denolle, M. A. (2019). Relating teleseismic backprojection images to earthquake kinematics. *Geophysical Journal International*, *217*(2), 729–747. doi: 10.1093/gji/ggz048

Yin, J., Denolle, M. A., & Yao, H. (2018). Spatial and Temporal Evolution of Earthquake Dynamics: Case Study of the Mw 8.3 Illapel Earthquake, Chile. *Journal of Geophysical Research: Solid Earth*, *123*(1), 344–367. doi: 10.1002/2017JB014265

Yin, J., Yang, H., Yao, H., & Weng, H. (2016). Coseismic radiation and stress drop during the 2015 Mw 8.3 Illapel, Chile megathrust earthquake. *Geophysical Research Letters*, *43*(4), 1520–1528. doi: 10.1002/2015GL067381

Yin, J., Yao, H., Yang, H., Qin, W., Jing, L.-Z., & Zhang, H. (2017). Frequency-dependent rupture process, stress change, and seismogenic mechanism of the 25 April 2015 Nepal Gorkha Mw 7.8 earthquake. *SCIENCE CHINA Earth Sciences*, *60*(4), 796–808. doi: 10.1007/s11430-016-9006-0

Yue, H., Simons, M., Duputel, Z., Jiang, J., Fielding, E., Liang, C., … Samsonov, S. V. (2016). Depth varying rupture properties during the 2015 Mw 7.8 Gorkha (Nepal) earthquake. *Tectonophysics*. doi: 10.1016/j.tecto.2016.07.005

Zhu, J., Canales, J. P., Han, S., Carbotte, S. M., Arnulf, A., & Nedimović, M. R. (2020). Vp/vs ratio of incoming sediments off cascadia subduction zone from analysis of controlled-source multicomponent obs records. *Journal of Geophysical Research: Solid Earth*, *125*(6), e2019JB019239.